TECHNICAL ARTICLE

Warm Aging of Pre-aged AA6013 Sheet and Its Relevance to Room Temperature and Warm Forming Applications—Experimental and Modeling Analyses

S. DiCecco, M. Di Ciano, N. Baghbanaghaie, S. Esmaeili, M.A. Wells, and M.J. Worswick

Warm forming has been shown to be an effective way to increase the formability of various aluminum sheet alloys. If applied to precipitation hardenable alloys, aging and/or coarsening may occur during heating and/or forming processes. As such, there is a potential to leverage the warm forming process to artificially age precipitation hardenable alloys. In this study, the aging characteristics of a pre-aged Al-Mg-Si-Cu alloy (designated AA6013-PA and comprising a 4 h, 100 °C pre-aging cycle following solutionization) were examined using: (i) room temperature tensile and (ii) bendability experiments, as well as (iii) elevated temperature tensile and formability experiments in the temperature range of 220-280 °C. In the pre-aged condition, the alloy exhibited very high work hardening, elongation and bendability. It was found that T6-like properties can be obtained with short duration secondary aging of the AA6013-PA starting temper (410 s at 235 °C), followed by a paint bake cycle (30 min at 177 °C). In such heavily aged conditions, the bendability is found to be moderate and consistent with a T6 temper. Bendability of the pre-aged alloy is shown to be enhanced by reducing the extent of aging, which may be beneficial for applications requiring energy absorption during crash, for example. In the pre-aged condition, AA6013 displayed a 55% improvement in room temperature formability, relative to the T6 condition, for near plane-strain loading using a Nakazima punch, although neither temper exhibited formability improvements through warm forming. The aging kinetics of AA6013-PA were determined from mechanical test data and used to calibrate an aging kinetics model. A strong obstacle model was used to relate precipitation state to yield strength, for artificial aging in the range 220-280 °C. The incremental strength increase due to exposure to an automotive paint cure cycle was also modeled and found to yield accurate results. Warm deformation, as well as room temperature deformation, were shown to enhance the paint bake response of the alloy, reducing the time to the peak aged condition by up to 14% for artificial aging at 177 °C.

1. Introduction

Recently, automotive manufacturers have exhibited renewed interest in warm forming as a potential manufacturing route for structural components made from medium to high strength aluminum alloys. This is reflected by recent research on warm formability of AA6111-T4 (Ref 1-3), AA6013-T6 (Ref 4, 5), and various other AA6xxx (Ref 6-9) and AA7xxx alloys (Ref 10-13). Warm forming subjects the material to elevated temperatures and deformation. For warm formed body-in-white (BIW) components, the material is also subjected to additional time at elevated temperature during paint curing operations. For a precipitation hardening aluminum alloy that is initially in a peak-aged, T6, temper, the warm forming operation will usually act to coarsen the existing precipitates; thus, the time at the forming temperature should be limited, as previously studied for AA6013-T6 (Ref 14). For a material initially in a naturally-aged (T4) or a pre-aged temper, the warm forming processing route may provide an opportunity to utilize the time at temperature during forming to further age the material prior to paint curing operations (Ref 15). Establishing the warm forming process parameters for both the shaping and in situ aging of precipitation hardenable aluminum alloys requires that the artificial aging kinetics of the alloy be evaluated. Furthermore, the effect of deformation on the kinetics of precipitation during warm forming and subsequent paint bake response, as well as the evolution of mechanical properties during processing, needs to be analyzed.

The artificial aging characteristics of AA6xxx alloys with various starting tempers have been studied extensively (Ref 16-34). In the typical artificial aging temperature range of 160-220 °C, there is consensus that pre-aging at temperatures of 80-100 °C enhances the artificial aging kinetics and final properties in comparison with the T4 starting condition (Ref 24, 27, 29, 30, 33). The GP zones formed during pre-aging are considered to be: (i) more resistant to dissolution upon exposure to subsequent artificial aging temperatures in com-

S. DiCecco, N. Baghbanaghaie, S. Esmaeili, M.A. Wells, and M.J. Worswick, Department of Mechanical and Mechatronics Engineering, University of Waterloo, 200 University Ave. W, Waterloo, ON N2L 3G1, Canada; and M. Di Ciano, Magna International Inc, Aurora, ON, Canada. Contact e-mail: sdicecco@uwaterloo.ca.

parison with clusters formed during natural aging (Ref 22, 24), and (ii) effective nucleating sites for the metastable β″ hardening precipitates in both non-Cu bearing (Ref 30) and Cu bearing (Ref 33) AA6xxx alloys. Despite the considerable knowledge regarding the effect of pre-aging on the artificial aging kinetics of AA6xxx alloys, the aging kinetics for temperatures greater than 220 °C have not been extensively reported in the literature, notably for high-Cu alloys. An et al. (Ref 34) studied the aging kinetics of a pre-aged Al-Mg-Si alloy at 230 and 250 °C. At elevated temperatures, both naturally aged and pre-aged alloys saw a decrease in yield and tensile strength for short exposure times; however, the pre-aged condition saw recovery in yield and tensile strength for longer durations, eventually exceeding the pre-aged strength at times beyond ∼ 150 s. Localized heating in excess of 230 °C of pre-aged deep-draw blanks was shown to improve drawability at room temperature relative to the baseline pre-aged condition.

While the effect of pre-strain (at room temperature), on the artificial aging kinetics of precipitation hardenable aluminum alloys has been studied to some extent, e.g., (Ref 35-37), there is less available literature for elevated temperature strain effects of relevance to warm forming. Teichmann et al. (Ref 38) artificially aged an Al-Mg-Si alloy at 190 °C, using both pre-deformed and simultaneously deformed and aged samples. Precipitates in the simultaneously deformed and aged samples were more finely and uniformly distributed than in the pre-deformed samples, and were of the post β″ type, providing evidence that the precipitation kinetics had been altered relative to the non-deformed specimens. The degree of precipitation strengthening was also reported to be larger for the simultaneously deformed and aged material, with the time required to reach peak hardness shortened. Di Ciano et al. (Ref 14) studied the effect of warm deformation on the coarsening of AA6013-T6. For test specimens that were warm deformed in the temperature range between 200 and 300 °C, up to an engineering strain of 8% and then held at the forming temperature for up to 330 s, there was a negligible effect of deformation on the subsequent yield and ultimate tensile strength of the material. Di Ciano et al. (Ref 14) further showed that specimens deformed at lower temperatures, 200 and 220 °C, exhibited work hardening during warm deformation and final yield strengths were increased relative to the un-deformed condition. Additionally, they showed that warm deformed (250 °C, 20% strain) and un-deformed specimens had similar final hardness levels after the paint cure process.

With respect to other precipitation hardening alloy systems, i.e., 2xxx and 7xxx Al alloys, Genevois et al. (Ref 39) studied the aging kinetics of AA2042-T351 (strain relieved and naturally aged) subject to deformation at room and elevated temperatures. A marked enhancement of the aging kinetics was observed from calorimetry on deformed specimens, for deformation at temperatures up to 230 °C. The resulting microstructure for specimens simultaneously heated and deformed contained precipitates with a lower aspect ratio than their un-deformed counterparts. Deschamps et al. (Ref 40) used in situ small angle x-ray scattering to study precipitation evolution during deformation at 160 °C for AA7449. During deformation, an enhanced precipitate coarsening rate was observed, which was 6-7 times larger than the rate for un-deformed samples. This enhancement appeared to be correlated with the degree of plastic strain within the specimens, was independent of strain rate and was attributed to the formation of non-equilibrium vacancies during plastic deformation that enhanced
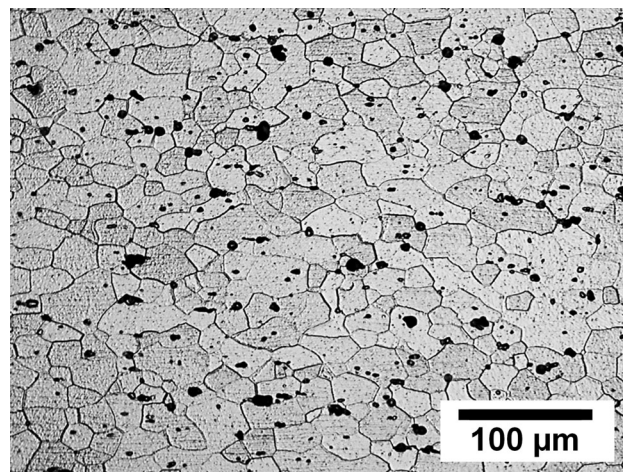

Fig. 1 As-received microstructure of AA6013-T6 sheet (etched with Keller's reagent for 30 s). The dark spots in the micrograph are etching pits

the kinetics of solute diffusion. After deformation ceased, the rate of aging decreased relative to the simultaneous deformation and aging condition; however, the rate of aging still remained higher than the un-deformed material by a factor of 2-3. This enhanced rate was attributed to pipe diffusion along dislocations formed during plastic straining.

While warm deformation can be expected to play a role in the subsequent precipitate evolution in all these aluminum alloy systems, various factors such as: (i) the initial precipitation state and alloy system, (ii) the deformation temperature and strain level, and (iii) the subsequent thermal processing steps will undoubtedly affect the material's behavior. For warm forming of pre-aged AA6xxx alloys, this effect warrants study. Thus, the primary objective of this work is to characterize the artificial aging kinetics of AA6013 in a pre-aged initial condition, for times and temperatures relevant to automotive warm forming processes. Secondary objectives are to examine the effect of warm deformation on the subsequent aging kinetics of AA6013 and conversely the aging effect (during heat up and forming) on the formability at warm temperatures.

2. Experimental Methods

The starting material used throughout this study was industrially produced 2 mm thick AA6013-T6 sheet, obtained from Arconic. Metallographic analysis of the as-received AA6013-T6 material showed that the grains were equiaxed, as shown in Fig. 1. The chemical composition of AA6013 was determined by Inductively-Coupled Plasma Atomic Emission Spectrometry, according to ASTM E1097-12 (Ref 41). The result of the analysis is given in Table 1.

Figure 2 serves to illustrate the thermo-mechanical processing histories considered in this work. To obtain a pre-aged (PA) temper of the alloy, samples were solutionized at 560 °C for 10 min in a fluidized sand furnace (FB-08C Fluidized Bath Furnace, Techne®), water quenched, and then aged at 100 °C for 4 h and water quenched a second time. Samples were stored in dry ice (− 78.5 °C) between the solutionizing and the 4 h aging steps, for a minimum of 12 h and maximum of 48 h. These samples are hereafter designated AA6013-PA. All

Table 1 Composition of AA6013 used in this work, in wt. %

	Al	Mg	Si	Cu	Fe	Mn	Cr	Ti	Zn
AA6013	Bal.	0.92	0.7	0.86	0.28	0.34	0.03	0.02	0.04
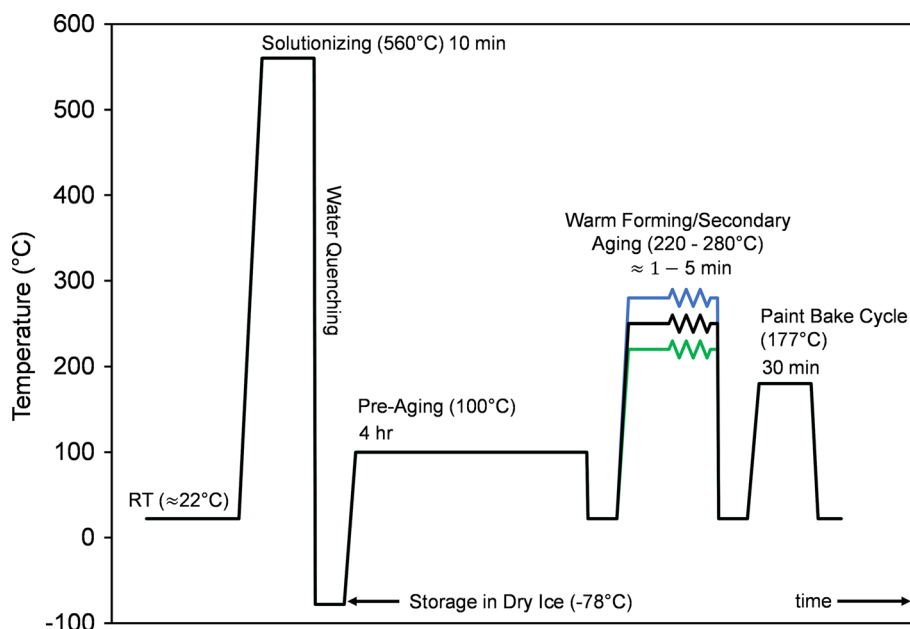
Fig. 2 Processing routes used for warm forming of pre-aged aluminum alloys. Note that dry ice storage was used in the current work to limit aging between the quenching and pre-aging cycles

samples were then stored in a freezer ($-20\ °C$) following pre-aging and prior to or between any deformation or heat treatments. The maximum time samples were stored in a freezer before testing was one month.

2.1 Mechanical Testing of Secondary Aged AA6013-PA Samples

ASTM-E8 sub-sized tensile coupons (Ref 42) were machined from the AA6013-PA sheet. The gauge length and width of the sub-sized specimens were 25 and 6 mm, respectively. The AA6013-PA samples were subjected to a secondary aging process (without deformation–deformation effects are addressed in the following section) in a fluidized sand furnace (FB-08C Fluidized Bath Furnace, Techne®) and quenched in room temperature water. Isothermal secondary aging treatments were conducted on the tensile coupons at the following temperatures: 220, 227, 235, 243, 250, 265, and 280 °C. The exposure times for these isothermal heat treatment times varied from 30 to 3000 s in duration. A subset of these tensile coupons was further treated with an additional laboratory aging process of heating at 177 °C for 30 min to simulate a paint bake cycle (PBC).

Following heat treatments, samples were tensile tested at room temperature with a 100 kN load frame (MTS Criterion™: Model 45). A 25 mm virtual extensometer was used to report strain values for stress–strain curves, acquired using digital image correlation (DIC)-based strain measurement. The cross-head speed for all tests was 0.0508 mm/s (corresponding to a nominal strain rate of $0.002\ \mathrm{s}^{-1}$) and each test condition was

repeated a minimum of three times. For each condition, the average yield strength and ultimate tensile strength were reported.

Stereoscopic digital image correlation was utilized for the acquisition of all reported strain measurements within this manuscript. With DIC, a temperature-stable random black on white speckle pattern was produced on the specimens using VHT Flame Proof© elevated temperature paint and a modified spray nozzle. Deformation of speckled samples was tracked by two 4 megapixel, 140 frames per second, FLIR Gazelle Camera Link cameras. The pixel density, in pixels/mm, varied as a function of the test setup, but was typically greater than 15 pixels/mm. Deformation and strain fields were analyzed using the Correlated Solutions Vic 3D© software package using a subset of 25-35 pixels, a step size of 2-4 pixels, and a Gaussian strain filter of 5 pixels. These analysis parameters influenced the minimum strain resolution and controlled the range over which strain averaging could be prominent (Ref 43-45). Sometimes referred to as the virtual strain gage length (VSGL) (Ref 46), the approximate minimum and typical regions of strain averaging in this work were 0.4 and 1.3 mm, respectively.

AA6013-PA specimens (40 mm by 40 mm by 2 mm) were also subjected to bending tests following the VDA 238-100 standard (Ref 47). Bendability, defined in ref. (Ref 48), is an important indicator of fracture resistance and is often used to assess the ability of a sheet metal to undergo hemming operations. Bendability can also be used to gauge the ability of a material to deform through progressive folding under crash

loading (Ref 49). For side impact structural beams, Kurz et al. (Ref 49) have found that the VDA bend angle correlates well with the amount of beam deflection (during 3-point bending) that can be realized prior to crack initiation. Additionally, they have reported that no cracking was observed for material conditions displaying VDA bend angles above 80°-100° for side impact beams subject to 150 mm of deflection (again, in 3-point bending). As per the VDA standard, a knife edge radius of 0.4 mm was used along with a punch speed of 20 mm/min. Teflon aerosol lubricant was used to lubricate the rollers prior to each test. Further details of the apparatus can be found in the publication by Cheong et al. (Ref 48). A threshold load drop of 30 N was used as the criterion for failure during the bending test, and the associated bending angle at failure was determined using DIC data. The failure threshold of 30 N corresponds to the standard for sheet metal less than or equal to 2.0 mm in thickness (Ref 47).

2.2 Warm Deformation of AA6013-PA

Warm tensile experiments were performed on the pre-aged AA6013 samples in order to characterize the extent of aging taking place during warm forming operations. In addition, warm forming experiments were performed to assess the effect of aging on formability, as well as to provide samples for calorimetry measurements examining the impact of warm deformation on the subsequent aging kinetics.

2.2.1 Warm Tensile Testing (Thermo-Mechanical Simulator). Warm tensile testing of AA6013-PA tensile samples was performed using a thermo-mechanical simulator (Gleeble-3500, Dynamic Systems Inc.). The purpose of the testing was to understand the effects of time and strain-rate at 230 °C, adopted here as a representative warm forming temperature, on the *in situ* flow response of the alloy in the -PA condition to complement the precipitation kinetics analysis of the warm bulk deformed sheet specimens.

To minimize thermal gradients along the length of the coupons, a grip length of 60 mm and a gauge length of 20 mm was used. Further details regarding specimen geometry are given in (Ref 14). Samples were warm deformed at 230 ± 2 °C. The test procedure was as follows: the sample was first heated (while subject to a small pre-load of 200 N) to the target temperature in 10 s, held at temperature for a predetermined hold time, and pulled to failure at a constant stroke rate. The *hold time* parameter was intended to characterize the effect of secondary aging at 230 °C on the subsequent at-temperature stress–strain response of the -PA temper. From a practical standpoint, different hold times of 5, 70 and 180 s were considered to reflect the range of pre-heating durations

within the context of industrial warm forming processes incorporating different heating processes. Nominal strain rates of 0.01/s and 0.1/s were tested to assess the strain rate sensitivity of the -PA temper at temperature. In total, six unique hold time and strain-rate conditions were tested at 230 °C.

Tensile strains were tracked using in situ DIC that was time-synchronized to filtered load curves output from the thermo-mechanical simulator. A 10 mm virtual extensometer was used to report strain values for the stress–strain curves. Note that during the heating and holding period, a displacement of about 0.25 mm was registered on all of the test specimens. This behavior was attributed to thermal expansion, since the stress level associated with the 200 N pre-load was only 16.7 MPa.

2.2.2 Formability Characterization of Sheet Specimens under Warm Forming Conditions. Formability characterization of the –PA and –T6 tempers was undertaken at elevated temperatures of 150 and 230 °C, in addition to room temperature. All testing was accomplished using a double-acting hydraulic press with tooling heated by embedded heater cartridges that were controlled with a closed-loop PID system, as described in (Ref 4, 5). Specimens were heated in situ using the heated tooling. From the time of clamping, it took three minutes for the samples to be heated to the target temperatures; however, heating was asymptotic and during the last 60-90 s the blanks were within approximately 20 °C or less of the prescribed temperatures.

Formability characterization was completed for the -PA and -T6 tempers. A 101.6 mm diameter Nakazima punch was used in formability testing per the ISO standard, as shown in Fig. 3. The formability was evaluated using a near-plane strain *dogbone* type geometry with a gauge width of 76.2 mm (3 in) and a die entry radius of 20 mm, per ISO 12004-2:2008. Plane-strain is typically the limiting condition in many forming operations and acts as a useful comparative metric when evaluating the formability of different sheet metals and forming conditions. A clamping force of 330 kN was applied to prevent material draw-in at elevated tempers. The punch speed during testing was 1.0 mm/s and lubrication between the punch and blank interface consisted of 2-3 layers of 0.127 mm Teflon® film. A more detailed description of the formability testing procedures may be found in DiCecco et al. (Ref 5).

In the formability testing, the Nakazima samples were tested to failure and digital image correlation techniques were used to capture the deformation gradients and corresponding strain fields within the samples over the duration of testing. All samples were tested with the rolling direction parallel to the sample length. Forming limit strains were determined from the acquired DIC data using a necking detection scheme that
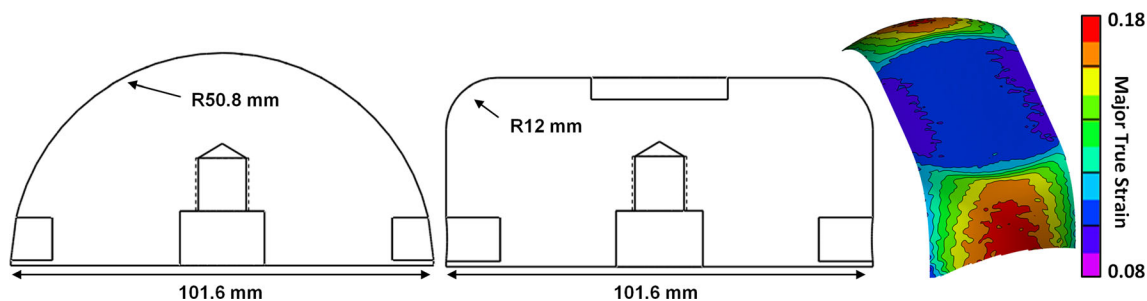

Fig. 3 Schematics of the Nakazima (left) and Marciniak (center) punches used for pre-straining and formability characterization, respectively. A typical DIC strain contour from pre-straining using the MK punch is shown on the right

determines when necking has occurred based on changes in the sample topology consistent with localization and necking, referred to herein as the curvature approach. The curvature approach applied in this work is termed the Enhanced Curvature Method (ECM) and was built upon the method developed by DiCecco et al. (Ref 5).

2.3 Warm Pre-Straining Experiments

Warm pre-straining experiments were performed using an annular Marciniak die-set (Fig. 3) in order to examine the effect of warm deformation on the subsequent aging response (during PBC, for example). The Marciniak punch promotes a region of uniform strain at the center of the sample that was suitable for subsequent harvesting of calorimetry samples. These pre-straining experiments were performed at room temperature (RT), 170 and 230 °C and utilized heated tooling with an inner diameter of 106 mm and die entry radius of 12 mm. The Marciniak samples were rectangular of width 50.8 mm and length 203.2 mm. The Marciniak punch had a 32 mm recessed hole (Fig. 3) machined in the center to promote uniform stretching over the punch. The rectangular samples were clamped between the dies using a force of 330 kN to prevent material draw-in.

The punch speed was 1.0 mm/s and motion was interrupted at punch depth of 24-26 mm which corresponded to a major true strain of approximately 0.1 ± 0.01 in the uniform deformation region for all test conditions, with a minor true strain of approximately -0.04, as determined using the DIC system. A typical strain contour from one of the pre-strained specimens is seen in Fig. 3. Specimens were heated following the same procedure as in the Nakazima warm forming operation with a 3 min heating time with asymptotic temperature rise toward the target temperature. Following pre-straining, samples from the uniform strain regions were sectioned for calorimetry experiments to evaluate the effect of deformation on the subsequent aging kinetics of the PA temper.

2.4 Calorimetry of AA6013-PA

To characterize the effect of deformation cycle on the precipitation process, Differential Scanning Calorimetry (DSC) experiments were conducted using a Netzsch DSC 404C apparatus and a constant heating rate of 10 °C/min within the range of 25-580 °C. The DSC tests were performed on the samples extracted from the center of the Marciniak specimens deformed at RT, 170 °C and 230 °C and the undeformed flange regions of the RT specimens with an average sample mass of 60 mg. Two repeated DSC tests were performed for each sample condition. For each testing condition, an alloy sample was placed in the test vessel and a reference pure aluminum sample of identical mass was placed in the reference vessel. The heat released or absorbed was recorded as a function of temperature corresponding to precipitation or dissolution reactions, respectively. To obtain the baseline, a second test was run with pure aluminum samples placed in both test and reference vessels. The net DSC trace was obtained by subtracting the data obtained from the reference material, i.e., pure aluminum, from the data recorded for the alloy sample.

To analyze the precipitation kinetics, Isothermal Calorimetry (IC) tests were conducted using a SETARAM C80 calorimeter, based on the methodology introduced by Esmaeili et al. (Ref 17, 24). Multiple pieces of the deformed and undeformed samples with a total mass of 930-970 mg were extracted from the center and flange regions, respectively, of the RT and warm deformed Marciniak samples. The calorimeter was first stabilized at the test temperature of 177 °C, then the samples were placed into the test vessel 20 s after data acquisition was started. Heat flow was recorded as a function of aging time at the constant temperature of 177 °C. The same IC test was completed on a pure Al sample with a total mass of 935 mg. The result of the pure aluminum run was then subtracted from the alloy sample run trace. The repeatability of the IC test results was checked by running at least two tests on each studied condition.

3. Results and Discussion

3.1 Warm Aging–Effect on Subsequent Room Temperature Mechanical Behavior

The evolution of the room temperature yield stress (YS), ultimate tensile strength (UTS), and toughness (integral of the tensile stress–strain response) of AA6013-PA after secondary aging at temperatures ranging from 220 to 280 °C is shown in Fig. 4. For material aged at 220 °C for longer durations of 1000-4000 s, the YS is slightly lower than the measured as-received (T6) YS (solid black symbol in figures), while the UTS is slightly higher. For short exposure times, the YS of the material does not decrease when aged at 250 °C and below, compared to the PA starting condition (open black symbol in figures). This behavior indicates that the 100 °C, 4 h PA treatment sufficiently stabilizes precipitates such that dissolution does not occur upon higher temperature exposure. For AA6013-PA exposed to secondary aging at 265 and 280 °C, there is a small decrease in the measured YS at the shortest exposure time of 30 s. Given the scatter in the data at 280 °C and 30 s, it is hard to conclude whether dissolution of precipitates occurs at this temperature. Regardless, due to the rapid aging kinetics at these temperatures, any dissolution which occurs upon exposure is quickly recovered by formation of new precipitates, as evidenced by the recovery of the YS past the original PA yield stress within 40 s. The UTS follows a similar trend as the YS at these short exposure times; however, the time required to recover the UTS is longer. While the scatter in the tensile toughness data is larger than the YS and UTS data, the trends are clear. For aging at 265 and 280 °C, the tensile toughness drops from the PA value to a level much closer to the T6 value for less than 100 s of exposure. At longer exposure times, the tensile toughness falls below that of the AA6013-T6 condition. For exposure at 250 °C, the tensile toughness after 100-400 s exposure remains higher than the T6 condition, although it does appear that at long exposure times the final toughness is equivalent to that of the T6 condition. For lower temperature exposures, i.e., 235 and 220 °C, the final tensile toughness remains greater than the AA6013-T6 condition up to the time required to reach peak strength at each temperature.

The effect of the PBC following secondary aging on the flow behavior of AA6013-PA is examined in Fig. 5. Here, a secondary aging temperature of 235 °C is considered, with secondary aging durations of 90-410 s (Fig. 5a, b, c, and d, respectively). This secondary aging temperature was selected since it offered a high level of toughness (Fig. 4c) and a strong difference in yield strength between short (90 s) and long
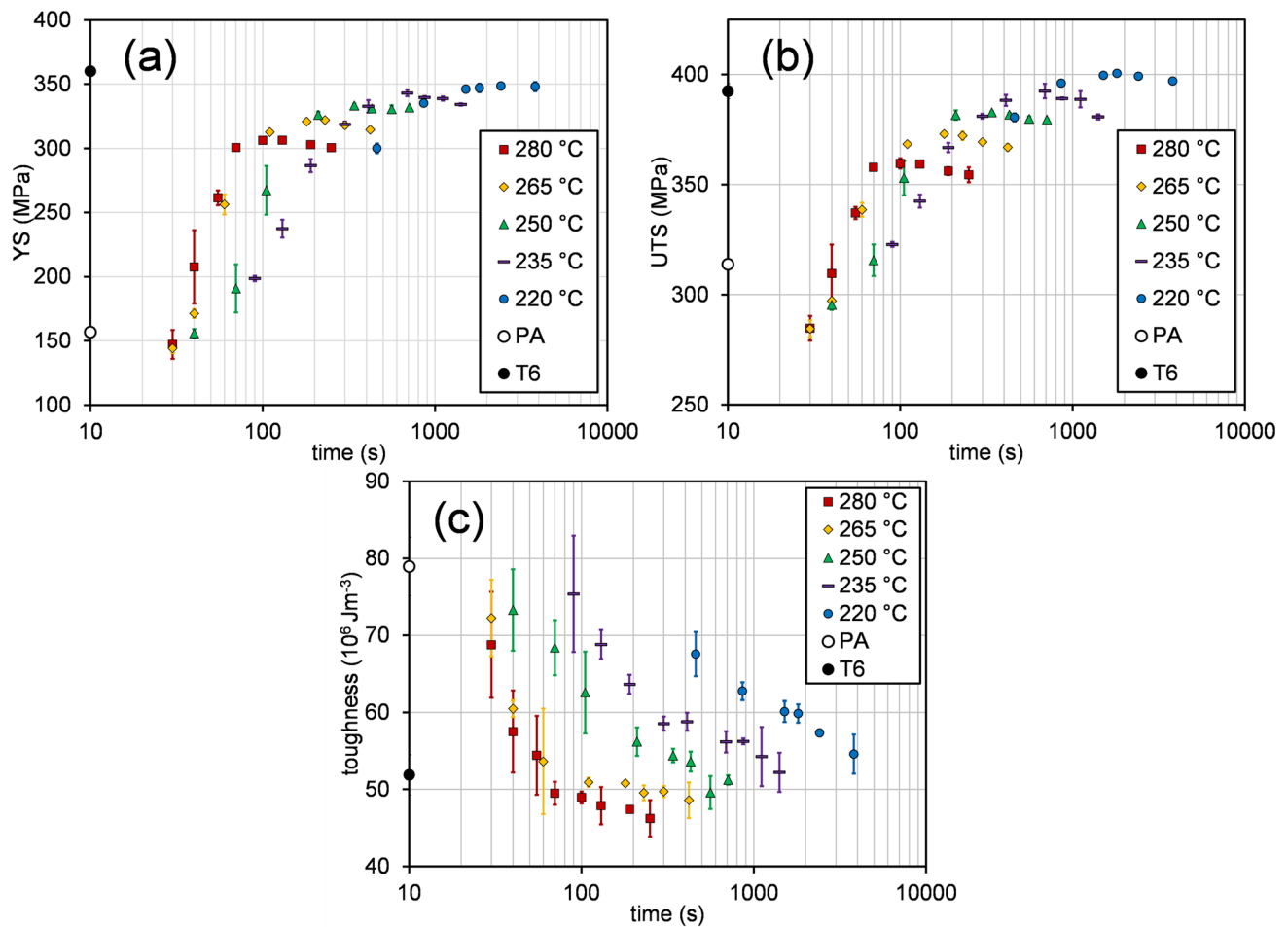
Fig. 4 Isothermal aging (between 220 °C and 280 °C) response of AA6013-PA: (a) yield stress (b) ultimate tensile strength, and (c) tensile toughness

(410 s) secondary aging durations. For reference, the stress–strain response immediately following PA, as well as that for AA6013 in the T6 peak aged condition are also plotted. The UTS following the PBC and short secondary aging times is very close to the UTS for AA6013 in the T6 condition, as illustrated in Fig. 5(a). Interestingly, the corresponding YS is relatively low compared to the T6 condition, resulting in a stronger work hardening response and higher elongation. As the secondary aging duration increases, the YS increases as a function of exposure time while the UTS stays relatively constant, thereby lessening the observed differences in the pre and post paint-baked engineering stress strain curves. Additionally, the change in strength due to the PBC alone decreases as a function of secondary aging time at 235 °C. For an initial exposure of 410 s, there is only a minor observable difference between the stress–strain responses of the material prior to and after the paint bake treatment (Fig. 5d). For all secondary aging times considered, from 90 to 410 s, the strain hardening rates and elongations of the pre- and post-paint baked specimens remain higher than the strain hardening rate and elongation in the T6 condition. This difference persists up to the peak strength condition shown in Fig. 5(d) (410 s exposure at 235 °C, plus PBC treatment). The lower yield strength levels (relative to the T6 condition) are likely a consequence of the difference in aging temperatures between the as-received T6 material, which would have been aged at temperatures lower

than 180 °C, and the aging temperature used in this series of tests, i.e., 235 °C. From Fig. 5, the aging temperature strongly influences the peak YS that can be obtained, which is a direct manifestation of the effect of temperature on the precipitate population (i.e., dependence on the metastable phase diagram (Ref 50)), as well as solute diffusivity.

The effect of aging duration and paint bake cycle on subsequent sheet bendability (fracture resistance) was also examined. These samples also considered an aging temperature of 235 °C and durations of 90-410 s. The bendability results for AA6013-PA aged at 235 °C are shown in Fig. 6a. The bendability is quite high in the PA condition and then decreases rapidly during the first 200 s of exposure at 235 °C, then more gradually between 200 and 400 s, approaching the T6 value for longer exposure durations. Thus, to achieve a bend angle greater than the AA6013-T6 condition, the secondary aging (warm forming) exposure time should be limited to less than 300 s. For exposure times less than or equal to 300 s there is a clear distinction between the pre and post PBC AA6013-PA conditions. Although the post PBC AA6013 still has a final bend angle greater than the AA6013-T6, in order to obtain a final bend angle greater than 80-100°, the lower range shown by Kurz et al. (Ref 49) to suppress fracture during automotive side impact, the secondary aging (warm forming) time must be kept less than 90 s. In Fig. 6b, the bend angle has been plotted against the strain hardening potential, defined here as the
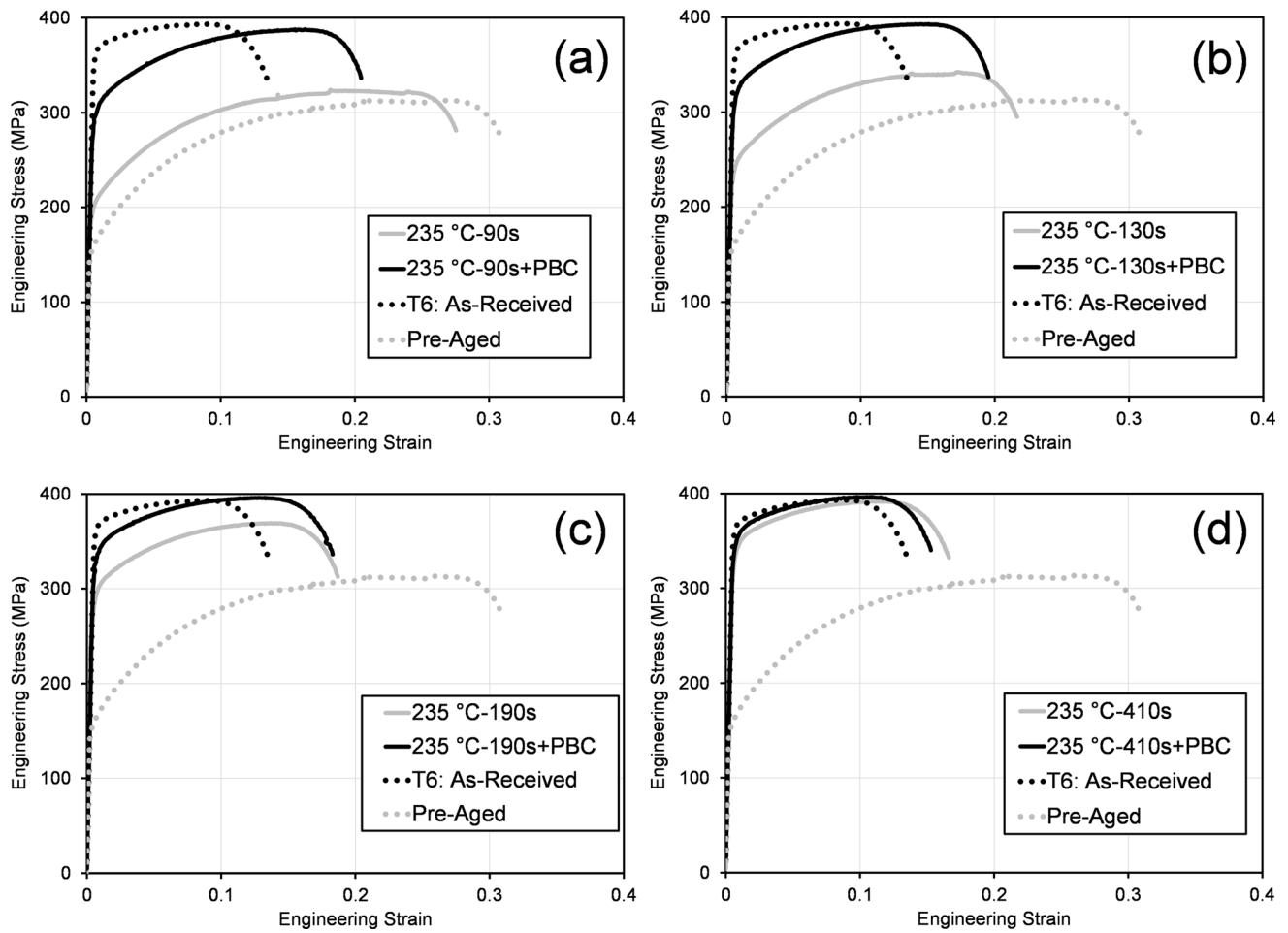
Fig. 5 Engineering stress vs. engineering strain of AA6013-PA before and after PBC, for specimens exposed to aging at 235 °C for (a) 90 s, (b) 130 s, (c) 190 s, and (d) 410 s (25 mm gauge length). Engineering stress vs. engineering strain corresponding to PA and T6 conditions area also included for comparison purposes
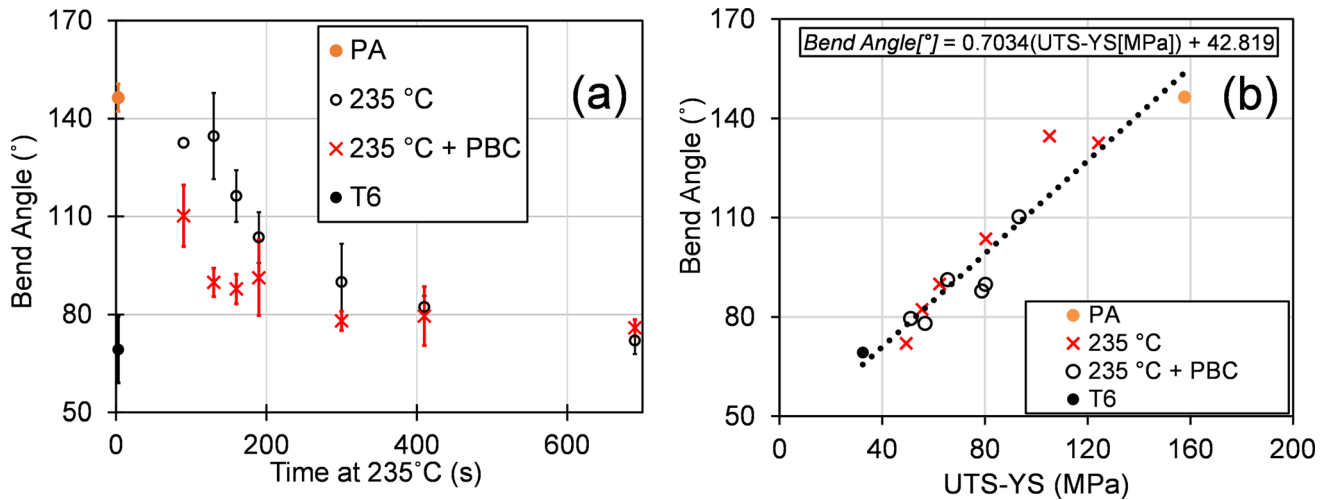

Fig. 6 (a) Bend angle as a function of duration of aging at 235 °C with and without PBC. Also shown are bending angles corresponding to PA and T6 conditions; and (b) hardening potential (UTS-YS) vs. bend angle for AA6013

difference in UTS and YS. The resulting linear trend shows a strong correlation, indicating that fracture resistance during crash can be improved by maintaining a strong work hardening potential.

The current results have potential practical implications related to the warm forming of 6000-series aluminum alloys using a pre-aged (-PA) starting temper. First, depending on the temperature, time, and strain imposed during warm forming
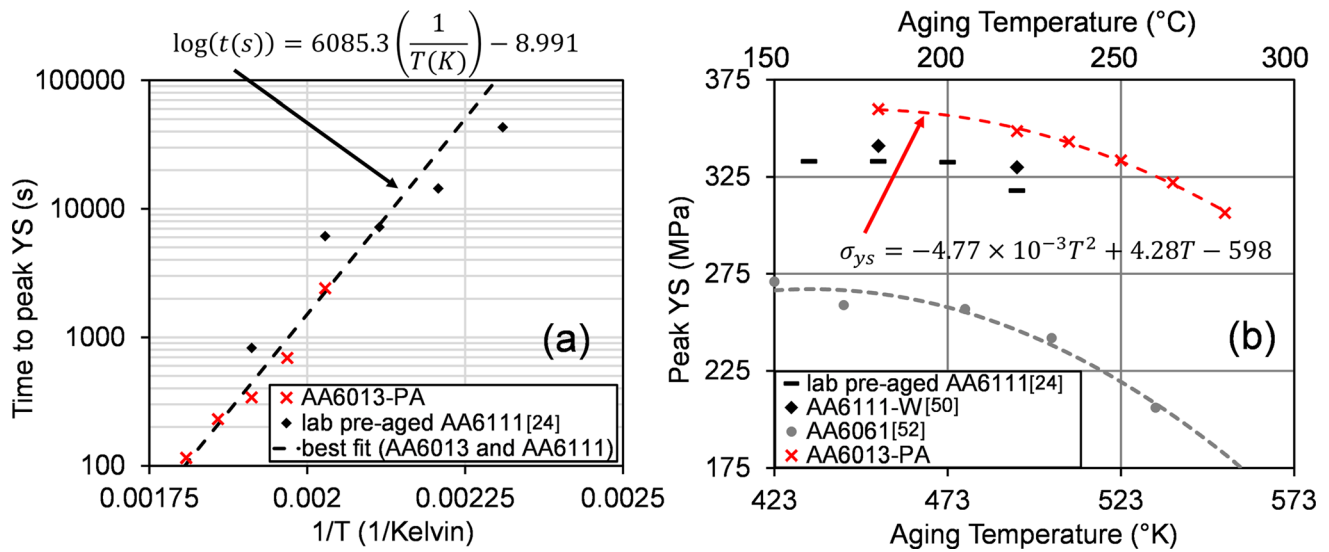
Fig. 7 (a) Time to peak yield strength and (b) peak yield stress as a function of aging temperature for isothermal aging of AA6013-PA. (Lab pre-aged AA6111 from Esmaeili and Lloyd (Ref 24), and AA6111-W data from Esmaeili (Ref 50). AA6061 from ASM Handbook (Ref 51) for reference)

and subsequent paint curing, UTS levels and, to a lesser extent, YS levels very close to T6 values can be readily achieved from the initial PA starting condition, followed by secondary aging (warm forming) and PBC. In a manufacturing setting, the time at temperature prior to forming, deformation during forming, and subsequent thermal treatments (such as the PBC in automotive parts) can be utilized to warm form AA6013-PA sheet and obtain parts with a high strength and parts with a high bendability (bend angle greater than 110° as in Fig. 6).

3.2 Warm Aging Kinetics

In order to examine the effect of temperature on aging at elevated temperatures, this section focuses on application of precipitation kinetics modeling to the current experiments in order to predict the increase in yield strength during pre-heating and to estimate the in situ increase in strength over the duration of the tensile tests. Here, the interaction between dislocations and rate of precipitation is neglected, essentially assuming that the precipitation process occurs under an undeformed state. The effect of warm deformation on the precipitation process is examined in Sect. 3.5.

3.2.1 Peak-aging Kinetics. The kinetics of late-stage precipitation (near the peak-aged condition) is examined by considering the temperature-dependence of the time (t_{peak}) to reach the peak YS, extracted from the data in Fig. 4a. For this purpose, the inverse of the time required to reach the peak YS ($1/t_{peak}$) is plotted in an Arrhenius form as a function of the corresponding temperature inverse (in 1/K), as shown in Fig. 7a. An Arrhenius-type relationship provides an excellent fit to the experimental data for the current AA6013 alloy, as well as to previously reported data on lab pre-aged (8 h of aging at 85 °C) AA6111 (Ref 24), despite the differences in the PA treatment. This result suggests that the rate of the late-stage artificial aging process, as represented by $1/t_{peak}$, can be modeled using an Arrhenius type formulation. Interestingly, an activation energy of 116.5 kJ/mol is obtained from the slope plot in Fig. 7(a) (after converting to natural logarithm and

multiplying by the universal gas constant, R). This value is close to the activation energy associated with the diffusion of the solute species (Mg, Si, Cu) in Al (i.e., 120-140 kJ/mol (Ref 50, 52), indicating that the artificial aging of AA6013-PA is independent of excess vacancies, unlike what has been reported for earlier stages of aging of AA6xxx alloys (Ref 19). This new understanding is expected to be very useful for future applications in alloy and process design, particularly for warm forming operations leveraging underaged alloys.

The peak YS as a function of aging temperature is summarized in Fig. 7(b) and compared to data for other AA6xxx alloys in the literature. Interestingly, it is observed that the trends of decrease in the peak YS with increase in aging temperature are very similar for all three alloys (AA6013, AA6111 and AA6061), regardless of their compositional differences (all within AA6xxx limits) and prior aging histories. Further study is needed to fully explain the reason for the observed similar trends regardless of the variations in the compositions and aging histories. For the current work, an empirical relationship between the peak yield strength of AA6013-PA and the aging temperature was determined, given by Eq 1.

$$\sigma_{ys}(T[K]) = -4.77 \times 10^{-3} T^2 + 4.28T - 598 [\text{MPa}] \quad \text{(Eq 1)}$$

3.2.2 Reverse Calculation of Precipitation Kinetics. A methodology is introduced here to reverse-calculate the kinetic parameters for precipitation hardening of pre-aged AA6013 alloy using the yield strength modeling approach developed by Esmaeili and Lloyd (Ref 23) and a limited set of YS data for the alloy. Accordingly, the formulations that relate the evolution of the yield strength of the material, σ_y, to the strengthening components σ_i, σ_{ss}, and σ_{ppt}, representing the intrinsic, solid solution, and precipitation hardening contributions, respectively, and through them to the relative volume fraction of precipitates, f_r, are as follows:

$$\sigma_y = \sigma_i + \sigma_{ss} + \sigma_{ppt} \quad \text{(Eq 2)}$$

$$\sigma_{ppt} = C_1(f_r)^{1/2} \qquad \text{(Eq 3)}$$

$$\sigma_{ss} = \sigma_{ss,o}(1 - \alpha f_r)^{2/3} \qquad \text{(Eq 4)}$$

Equation 3 is based on the strong obstacle assumption (Ref 15), which has been shown to work well for YS modeling of AA6xxx alloys for various starting tempers (Ref 15, 21, 23). The constant parameter C_1 in Eq 3 is a function of the precipitate volume fraction at the peak-aged condition (Ref 15), and thus is expected to change with a change in the aging temperature, as dictated by the alloy's metastable phase diagram. Using the empirical Eq 1 and assuming $\sigma_{ss} = 0$ (Ref 15, 50) for the peak-age condition, and $\sigma_i = 10$ MPa (Ref 16), C_1 can be found as a function of aging temperature:

$$C_1(T[K]) = -4.77 \times 10^{-3}T^2 + 4.28T - 608[MPa] \qquad \text{(Eq 5)}$$

In Eq 4 The constant parameter $\sigma_{ss,o}$ is related to yield strength of the solutionized and quenched material and $\alpha = 1$ (which matches the assumption of $\sigma_{ss} = 0$ at the peak aged condition) (Ref 15, 23).

The evolution of the YS of the pre-aged alloy with time at the artificial aging temperature is dictated by the relationship between f_r and temperature. For an isothermal aging process, the relationship is modeled as (Ref 15):

$$f_r = 1 - (1 - f_{r,o})\exp(-(kt)^n) \qquad \text{(Eq 6)}$$

where $f_{r,o}$ is the initial relative volume fraction of precipitates of the pre-aged material, t is the isothermal aging time, exponent n is a kinetic parameter, assumed to be independent of temperature, but typically dependent on the growth morphology of the precipitates, and k is the temperature-dependent aging kinetic parameter which follows an Arrhenius form with temperature:

$$k = k_o\exp\left(-\frac{Q_a}{RT}\right) \qquad \text{(Eq 7)}$$

where Q is an equivalent activation energy, k the pre-exponential constant, T the aging temperature in K, and R the universal gas constant (8.314 J/mol K).

To reverse calculate kinetic parameters n, Q_a and k_0, first Eq 1, 2, 3, 4, 5 and 6 and the YS data reported in Fig. 4a are used to obtain a set of data points for f_r (T,t). To account for sample heating effects, a value of 30 s was subtracted from all experimental aging times; and subsequent kinetic data was fit to the offset aging times. These data sets are then plotted in the following form to determine n and k for each aging temperature:

$$lnln\left(\frac{1 - f_{r,o}}{1 - f_r}\right) = nlnt + nlnk \qquad \text{(Eq 8)}$$

The values for k_o and Q_a are then determined via an Arrhenius plot of k, as shown in Fig. 8, following the methodology outlined in (Ref 24).

The resulting kinetic parameters are given in Table 2. The value of 1.3 reported for n in Table 2 is the average of the values obtained for the temperature range of 220-280 °C and is very similar to the values previously reported by Esmaeili and Lloyd (Ref 24) for modeling the kinetics of aging in AA6xxx-

Table 2 Aging kinetics and strength model parameters for AA6013-PA material

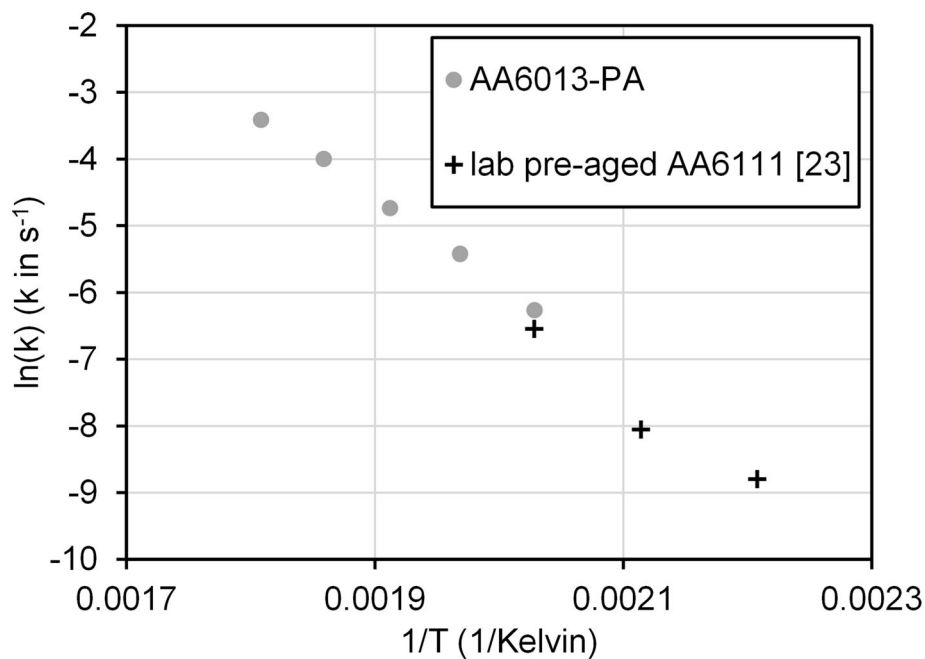| Variable	Value	Unit
Qa	1.08E + 02	kJ/mol
ko	6.00E + 08	s^{-1}
σ_i	10	MPa
σ_{sso}	40	MPa
α	1	
n	1.3	
f_{ro}	0.12	

Fig. 8 Arrhenius plot for AA6013-PA material, compared with data from lab pre-aged AA6111 from Esmaeili and Lloyd (Ref 24)
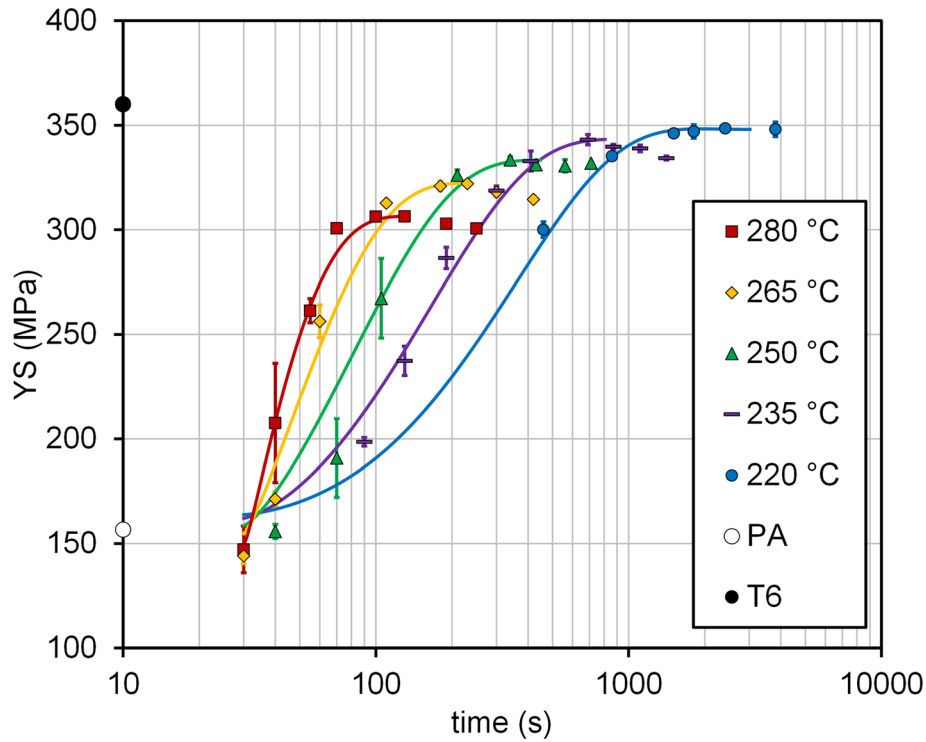
Fig. 9 Comparison of experimentally obtained data and model fit for the YS evolution of AA6013-PA during subsequent isothermal aging at the indicated temperatures

PA alloys ($n \cong 1.3$). The value obtained for Q_a, is also very similar to the value obtained by Esmaeili and Lloyd (Ref 24) using isothermal calorimetry on lab-pre-aged AA6111, and close to the value obtained from the analysis of the $1/t_{peak}$ data (116 kJ/mol) in Fig. 7(a).

The age hardening model predictions of yield strength and the corresponding experimental data are plotted in Fig. 9. Overall, the model captures the isothermal artificial aging behavior of AA6013-PA rather well.

3.3 Yield Strength Modeling: Paint Bake Response of AA6013-PA

To assess the precision of the fit kinetic parameters, as well as extend the range of applicability to include yield strength modeling of multi-step aging processes, additional heat treatments and analyses were performed.

Equation 2, 3, 4, and 5 and the kinetic parameters obtained in Sect. 3.2.2 (Table 2) are used to model the YS evolution of AA6013-PA during warm aging followed by paint bake cycling (PBC) processes. The warm aging temperatures are 227, 235, and 243 °C and the PBC has been simulated as a subsequent aging step at 177 °C for 30 min. For a multi-step aging treatment, fr is modeled using the following relationship (Ref 23):

$$f_r = 1 - \left(1 - f_{r,o}\right)\exp\left[-\sum_i k_i^n \left(t_i^n - t_{i-1}^n\right)\right] \quad \text{(Eq 9)}$$

where k_i is a temperature dependent $\left(k_i = \left[\frac{f(T_i)}{n}\right]^{1/n}\right)$ kinetic parameter, and t_i, T_i, are the values of time and temperature at discretized points i along the non-isothermal temperature history. The modeling results, along with the measured values of yield strength are shown in Fig. 10(a), (b), and (c). For the

aging temperatures of 227 and 235 °C, the yield strength predictions before and after PBC match the experimental data with very good accuracy. At the higher aging temperature of 243 °C, the model predictions prior to PBC are also of good accuracy; however, the predicted yield strength after PBC is slightly underestimated. In general, the multi-step process of warm aging plus paint baking is captured to within 10% of the experimentally measured quantities.

3.4 Warm Deformation–Hold Time and Strain Rate Effects

The elevated temperature (230 °C) engineering stress–strain response of AA6013 in the pre-aged condition is presented in Fig. 11(a) for a range of heating profiles and strain rates, while Fig. 11(b) shows the corresponding true stress versus effective plastic strain curves for each condition. These experiments were performed primarily to understand the effect of aging during pre-heating and warm forming on the mechanical response of the alloy during warm forming. Stress–strain curves for hold times of 5, 70, and 180 s were obtained for nominal strain rates of 0.01 and 0.1 s^{-1}. The different hold times prior to tensile testing serve to characterize the effect of secondary aging during heating on the "at-temperature" tensile response of the PA temper. These times reflect the range of "time at-temperature" in industrial applications in warm forming, spanning longer duration conventional furnace heating versus rapid contact or IR heating, as well as accounting for transfer times between the furnace and forming tools.

The yield strength at 230 °C is summarized in Table 3 and plotted in Fig. 12 for both strain rates as a function of hold time, from which it can be seen that the yield strength increased significantly with the hold time. In order of ascending hold time for the lower strain rate, yield strengths of approximately 130, 179, and 236 MPa were observed, with relatively low scatter as
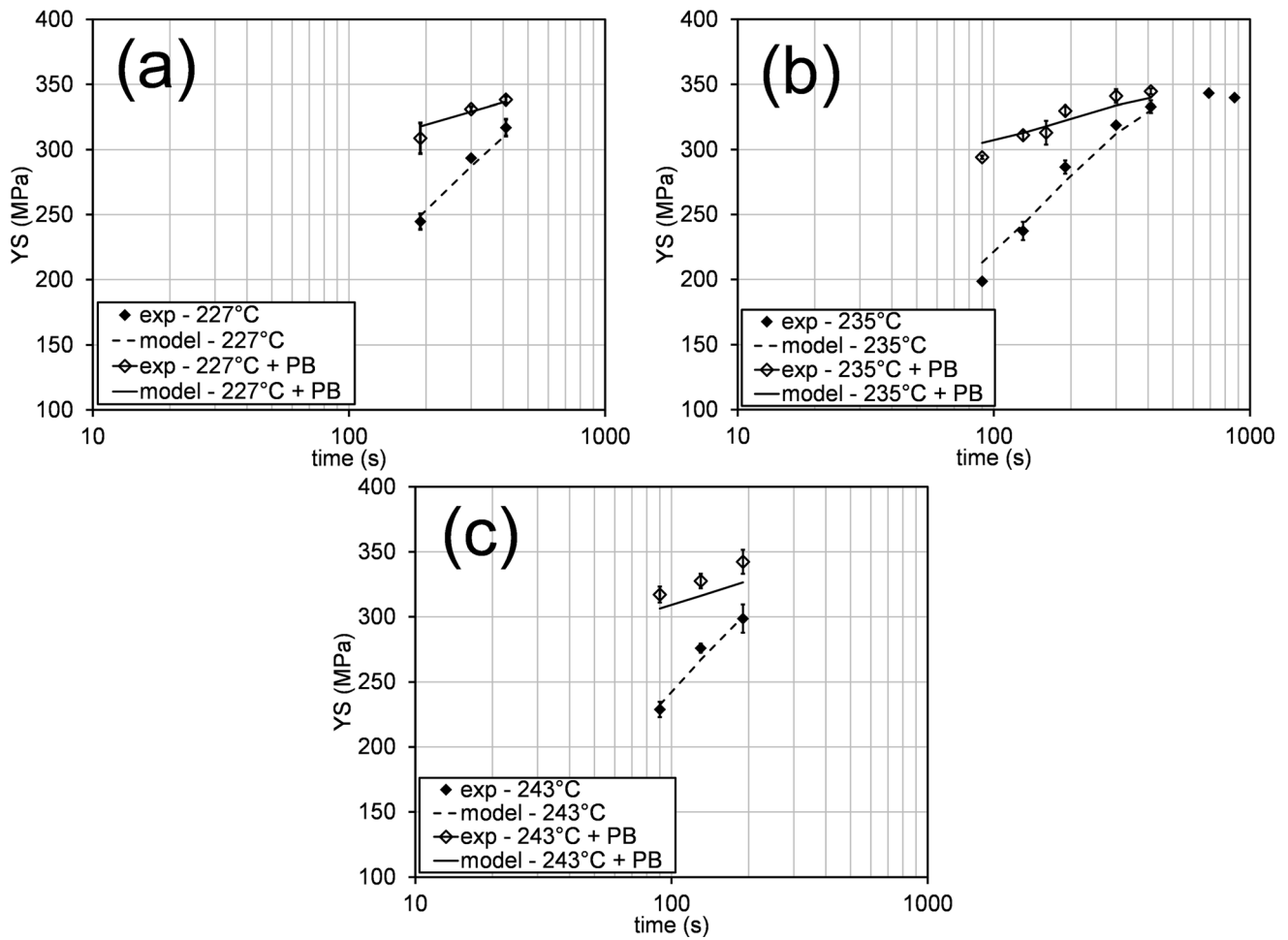
Fig. 10 Yield stress of AA6013-PA exposed to secondary aging at (a) 227 °C, (b) 235 °C or (c) 243 °C with or without a PBC (177 °C for 30 min). The horizontal axis corresponds to the secondary aging duration
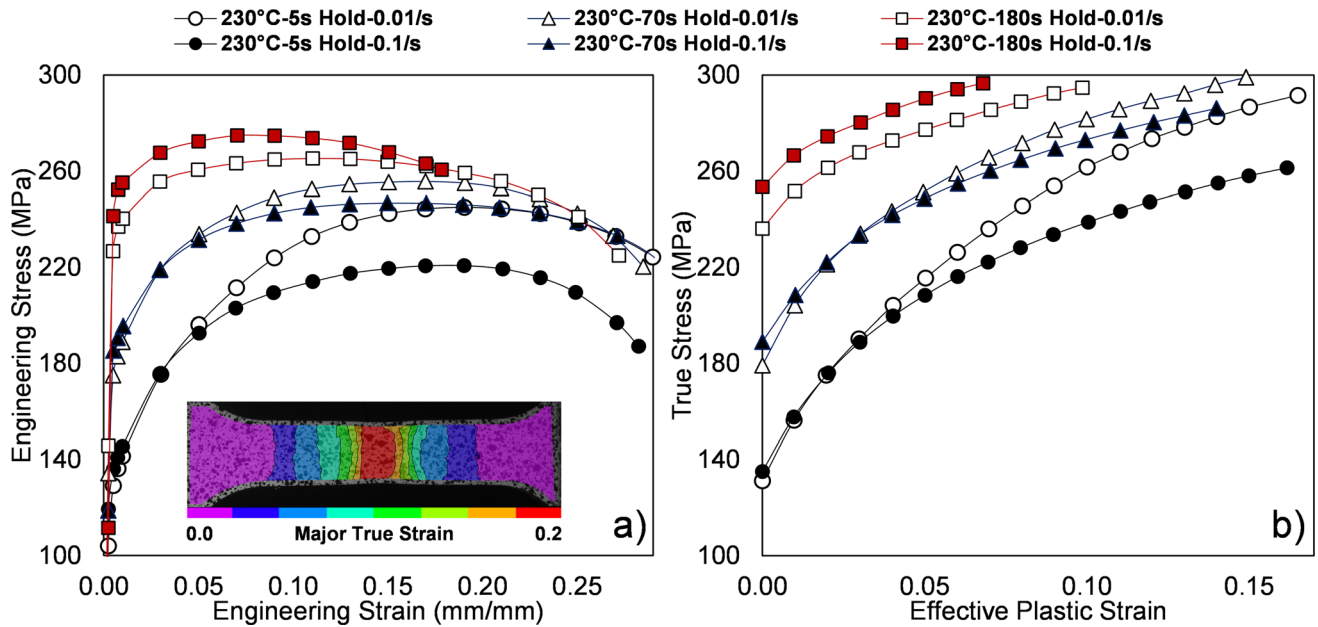

Fig. 11 Tensile response of AA6013-PA at 230 °C as a function of hold time following heating to temperature and strain rate. Samples were heated rapidly using a thermomechanical simulator and held for various times at 230 °C (5, 70, and 180 s) prior to tensile testing. Note that representative curves are plotted for each test condition and that the scatter is relatively low, as captured in Table 3

Table 3 Summary of AA6013-PA tensile response to hold time and strain-rate effects at 230 °C, with corresponding standard deviations included in brackets

| Hold time, s	Strain rate, s⁻¹	Time to yield, s	YS, MPa	Time to UTS, s	UTS, MPa	Uniform Elongation	n4-6%
5	0.01	1.25 [0.05]	130 [0.9]	12.58 [0.25]	245.3 [0.2]	0.18 [0.01]	0.27 [0.01]
5	0.10	0.15 [0.01]	132.1 [5]	1.13 [0.01]	221 [0.5]	0.18 [0]	0.2 [0]
70	0.01	1.79 [0.29]	178.7 [1.3]	11.01 [0.41]	255.9 [0.4]	0.16 [0]	0.16 [0]
70	0.10	0.21 [0.03]	188.2 [2.8]	1.12 [0.05]	247.1 [2.5]	0.16 [0]	0.14 [0]
180	0.01	2.76 [0.01]	235.6 [3.2]	8.74 [0.45]	265.7 [1.2]	0.11 [0.01]	0.08 [0]
180	0.10	0.32 [0.02]	250.1 [2.9]	0.89 [0.06]	275.5 [1.6]	0.08 [0.01]	0.08 [0.01]
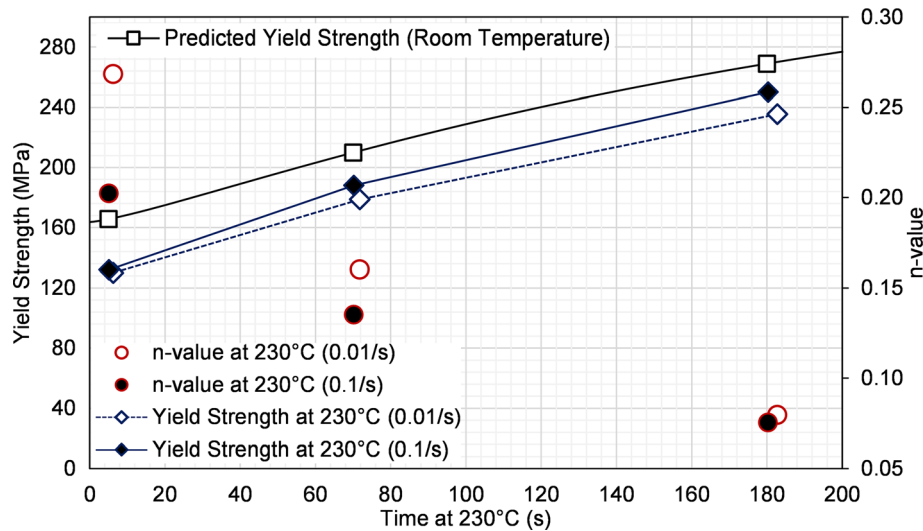
Fig. 12 Yield strength and strain-hardening exponent of AA6013-PA at 230 °C as a function of strain rate and time at temperature (hold time) prior to testing. The predicted room-temperature yield strength as a function of aging time at 230 °C (Sect. 3.2.2) is also plotted

shown in Table 3. This increase in yield strength with increased hold time can be attributed to secondary aging during the heating and hold period. For comparison purposes, the predicted increase in room temperature yield strength, obtained using the kinetics model developed in Sect. 3.2.2, is also plotted in Fig. 12. While these predictions are for room temperature, it can be seen that the aging predictions scale well with the measured increase in elevated temperature yield strength as the hold time increases.

For all hold times, the higher strain rate led to an increase in YS relative to the lower strain rate that evolved from 2 to 14 MPa for the shortest to the longest hold time. A positive difference in YS for the imposed increase in strain rate indicates a positive strain-rate sensitivity at yielding at 230 °C that was most pronounced for the longest hold time.

The hardening behavior after yielding for the longest hold time of 180 s also exhibits positive strain rate sensitivity, as seen in Fig. 11b, which is consistent with other stable (solution strengthened or peak aged) aluminum alloys at elevated temperature (Ref 4, 5, 7). Of particular interest in the current results, the strain hardening response at strains beyond yielding for the shorter 5 and 70 s hold time experiments exhibits a seemingly negative strain rate sensitivity. To elaborate, in Fig. 11b, the lower rate curves at 5 and 70 s exhibit a higher degree of hardening, overtaking the strength of the higher strain rate curves after approximately 3-4% tensile strain. To further examine the effect of strain rate on hardening rate, the

hardening exponent (*n-value*) was calculated for all test conditions for effective plastic strains in the range of 0.04-0.06 and is plotted in Fig. 12. For a hold time of 5 s, the average *n*-values for the 0.01/s and 0.1/s rates were 0.27 and 0.20, respectively, which again reflects the negative rate sensitivity of the hardening response (lower hardening at higher strain rate) observed in Fig. 11. For the 70 s hold time, the *n*-values were somewhat lower and still exhibited a mild negative rate sensitivity, with *n*-values for the lower and higher strain rates being 0.16 and 0.14, respectively. For the longest hold time of 180 s, the calculated *n*-values were both effectively 0.08 for the lower and higher strain rates; thus, the positive strain rate sensitivity observed at yielding (Fig. 11) is preserved up to the UTS for both rates for this condition.

The decrease in the degree of hardening observed at higher rates of strain for shorter hold times is somewhat surprising since aluminum alloys typically exhibit an increase in work hardening with increases in strain rate at elevated temperatures. The overall hardening response captured by the calculated *n*-values in Fig. 12 has several components, the first being conventional work hardening due to plastic strain accumulation. There will also be an age hardening contribution during the tensile test that will be larger at lower strain rates due to the associated increase in the test duration (Table 3) leading to longer times at elevated temperatures. This effect is most pronounced for the PA temper and shorter hold times for which the extent of secondary aging prior to the start of the tensile test
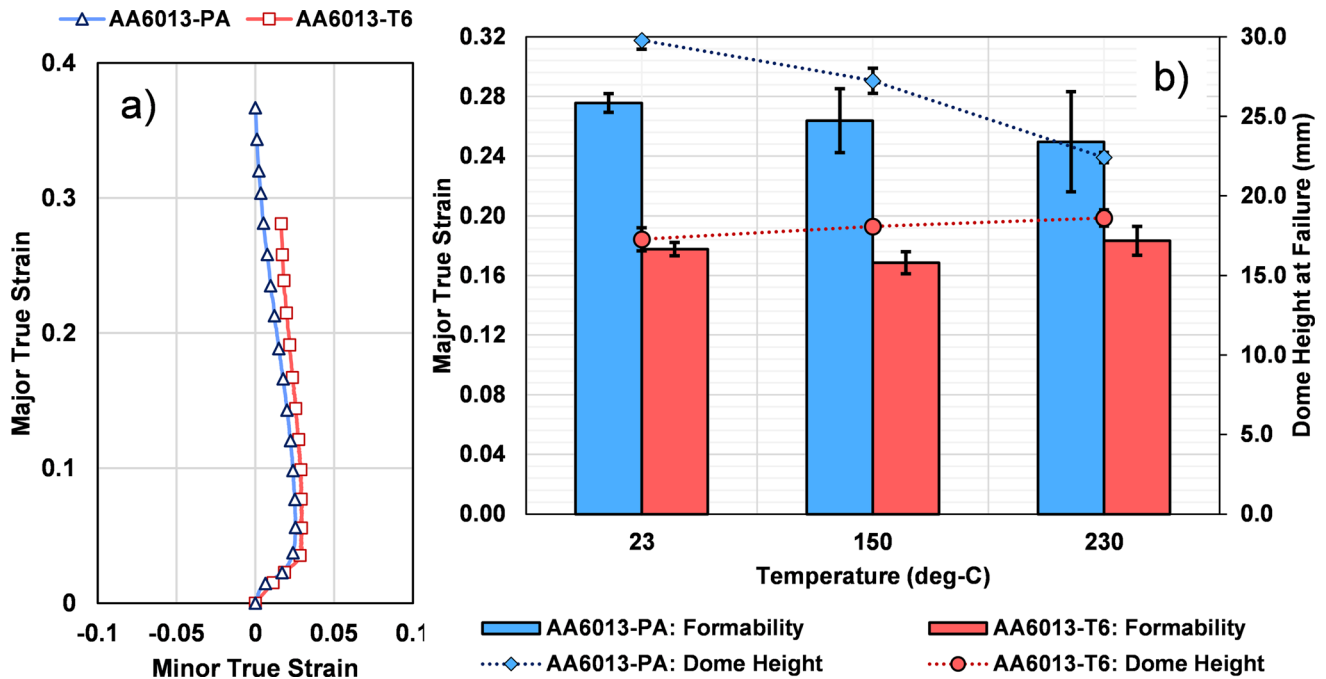
Fig. 13 (a) Room temperature strain paths for AA6013–PA and –T6 tempers and (b) major limit strains and average dome heights at failure for the two tempers as a function of temperature

is lower, as reflected by the YS data in Fig. 12. The effect of in situ aging during the elevated temperature tensile tests can be estimated using the kinetics model (Eq 2, 3, 4, and 5) and kinetic parameters obtained in Sect. 3.2.2. For instance, for the tensile tests using a 5 s hold time, the aging contribution to the room temperature yield strength due to in situ aging during testing at 0.01 s^{-1} would be 9-10 MPa. This increase in stress at least partially accounts for the greater degree of hardening observed in the lower strain rate data in Fig. 11. In contrast, the in situ aging over the short duration of the higher rate test (0.1 s^{-1}) would be negligible.

3.5 Warm Formability of PA and T6 Tempers

The formability of AA6013 was characterized in the PA and T6 tempers under isothermal conditions at room temperature, 150, and 230 °C, at a stroke rate of 1.0 mm/s, using dog-bone samples meant to approximate a plane strain loading condition (which is typically the lowest point on a forming limit curve). Representative strain paths taken at room temperature for each temper are plotted in Fig. 13(a). The strain paths were acquired from the necking region on each specimen over an approximate area of 1 mm^2 using DIC techniques and are plotted up to the image before fracture. Both strain paths demonstrate typical Nakazima characteristics, starting with biaxial bending as the blank wraps around the hemispherical punch geometry, followed by near-plane strain stretching controlled by the blank width and lubrication condition.

The measured plane strain limit strains, as a function of forming temperature and initial temper, are plotted in Fig. 13(b). Also plotted are the dome heights at onset of fracture for each case. At room temperature, the major true limit strain of the PA temper was 0.28 ± 0.01, which is, on average, a 55% improvement over the RT limit strain for the T6 temper. This significant formability improvement associated with the

PA temper is attributed to the much stronger work hardening (n-value) relative to the T6 temper, as is evident in Fig. 5.

The T6 temper shows very little difference in formability with temperature for the range of test temperatures, as is the change in dome height. Note that the scatter in the test results (n_{min} = 3) was low for all conditions and testing of the T6 baseline temper was generally repeatable.

In general, the elevated temperature formability of the PA temper was found to decrease relative to RT while the repeatability also decreased, as evidenced by the increase in the scatter of the measurements. The final dome heights prior to fracture further confirm this trend, with a decrease from 30 mm to approximately 23 mm from RT to 230 °C. In Sect. 3.3, it was observed that the hardening rate of the PA temper at 230 °C varies significantly as a function of time at temperature and that a short heating cycle might be leveraged to increase formability; however, in the warm formability testing conducted in the present study, heating rates were limited to the contact heating rates of the tooling. In total, 3 min was required to heat the specimens to the target temperatures, with 60-90 s of asymptotic heating. Thus, the current 230 °C warm formability experiments on the PA temper reflect a condition that likely falls somewhere between the 70 and 180 s hold times in the warm tensile tests for which n-values of approximately 0.16 and 0.08 were measured, respectively, as opposed to the 5 s hold time for which an effective n-value of approximately 0.27 was measured. The higher n-value for short heating times suggests that improvements in warm formability may be possible using duration heating; however, fast heating for the formability experiments was not available in the current work.

Warm forming was not found to be beneficial for the PA temper using the current specimen heating approach (duration); however, the room-temperature formability of the PA temper was excellent and showed a significant improvement over the peak aged formability. From Fig. 5 it can be seen that the PA
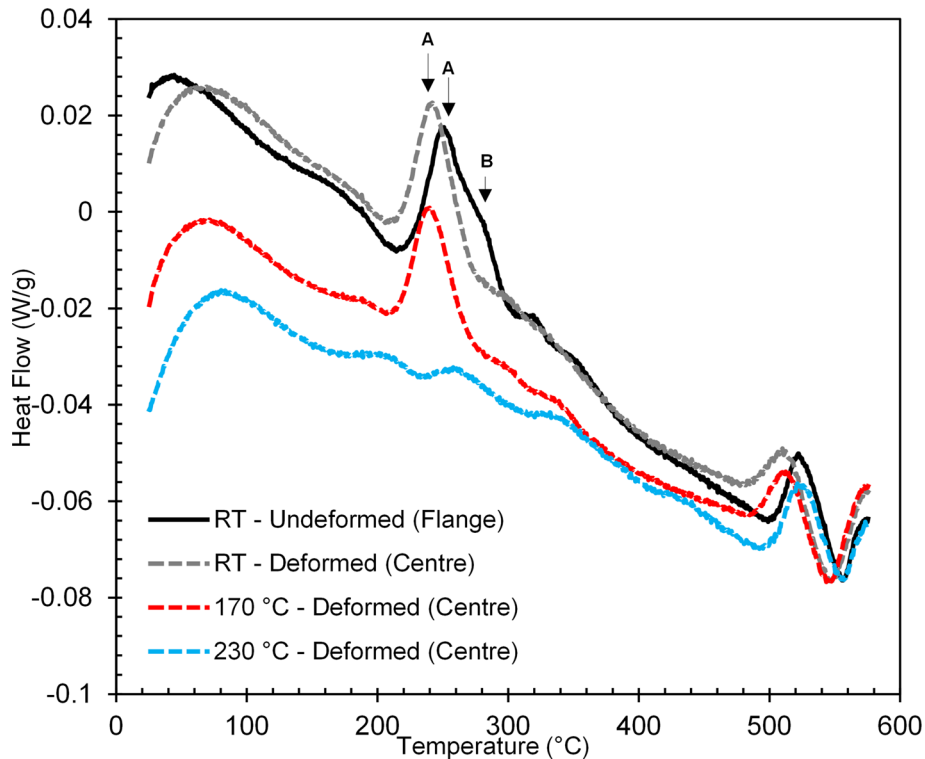
Fig. 14 DSC traces of AA6013-PA samples deformed using a Marciniak punch at various temperatures: Room Temperature (RT), 170 °C, and 230 °C. DSC trace of an undeformed AA6013-PA sample (taken from the flange region of a RT Marciniak test sample) also shown for comparison

temper, after exposure to a thermal cycle of 410 s (6.8 min) at 235 °C, will have a stress–strain response in-line with the baseline T6 temper (independent of a subsequent paint-bake.) Thus, the PA starting temper, when combined with a relatively short secondary aging cycle after forming, offers a T6 final strength level with a 50% improvement in formability. This cycle could be further optimized using the calibrated kinetics model in Sect. 3.2 based on desired final strength and ductility characteristics or for different heating cycles based on furnace capabilities.

3.6 Effect of Warm Deformation on Aging Kinetics

The effect of deformation on the aging kinetics occurring during warm forming was examined by relative comparison of DSC traces of pre-strained AA6013-PA samples, deformed at RT, 170 and 230 °C, against a DSC trace of AA6013-PA without pre-strain or temperature exposure. Deformed samples were extracted from the center of the pre-strained Marciniak samples, while the undeformed sample was extracted from the flange of an RT Marciniak specimen. The DSC traces are presented in Fig. 14 for which the exothermic events have positive (upward facing) peaks and are associated with the formation of new precipitates, while endothermic events have negative (downward facing) peaks and indicate dissolution of existing precipitates. The exothermic peak between 200 and 300 °C (peak A) represents the precipitation event associated with the β'' phase which is the primary hardening phase in artificially aged AA6xxx alloys (23, 50). Three key observations can be made from examination of the DSC curves in Fig. 14. First, peak A is not present in the DSC trace of the sample deformed at 230 °C. This absence is attributed to the

fact that aging which occurred during sample heating and throughout the warm forming process at 230 °C may have brought the sample into a condition close to the peak aged (or T6) temper. As such, the DSC thermogram for the sample warm deformed at 230 °C only displays a broad endothermic trace and peak at $\sim$ 500 °C, corresponding to dissolution of the equilibrium β (Mg_2Si) phase. As a result, for the specimen deformed at 230 °C, any potential effects due to deformation cannot be readily discerned from the DSC trace alone. Second, for the samples deformed at room temperature and 170 °C (dashed gray and red lines in Fig. 14), the temperature associated with the maximum heat flow of peak A (and hence maximum rate of reaction) was shifted to a lower temperature relative to the DSC trace for the undeformed sample (black solid line). This temperature shift indicates that the precipitation process in the deformed samples was accelerated relative to the undeformed baseline. Finally, the absence of a secondary exothermic peak (peak B) in the deformed samples relative to the undeformed sample (secondary peak at temperature of $\sim$ 280 °C) indicates that in addition to rate effects, deformation (at room temperature and warm temperatures) may alter the ratio of precipitate types which form during the aging process (β'' and Q'). A similar observation has been made for copper-free 6xxx alloys pre-deformed at room temperature, see Yassar et al. (Ref 36, 37).

To quantify the extent of kinetic enhancement as a result of warm deformation, isothermal calorimetry was conducted on the same series of samples deformed with the Marciniak punch at room temperature, 170 and 230 °C and compared with corresponding undeformed samples using the protocol defined in (Ref 17). All IC tests were conducted at a test temperature of
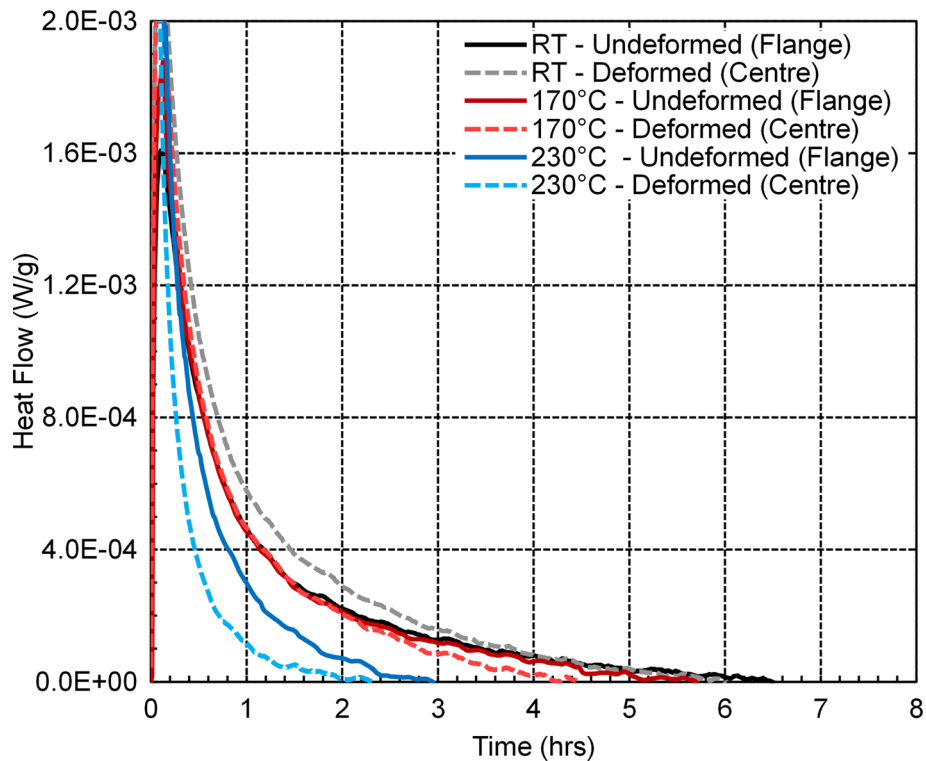
Fig. 15 IC traces of AA6013-PA samples deformed using a Marciniak punch at various temperatures: room temperature (RT), 170 °C, and 230 °C. IC traces of an un-deformed AA6013-PA samples (taken from flange region of Marciniak test samples) are also shown for comparison

177 °C, to reflect typical paint curing temperatures used in automotive BIW applications. Representative IC traces, given as normalized heat flow (W/g) as a function of test time, are shown in Fig. 15. For a precipitation reaction, the released heat gives rise to an exothermic heat event during the IC run and is measured during the IC test. As the reaction proceeds to completion, the rate of the heat release approaches zero. In the current work, reactions were recorded as complete at time t_f when the measured rate of heat flow dropped below 10^{-5} W/g. For precipitation hardenable Al alloys, it has been reported that the values of t_f obtained from IC tests are consistent with the times required to reach the peak-aged condition (Ref 17). Additionally, the area under each IC trace shows the amount of heat released due to the precipitation process and can be used to compare the extent of precipitation for specimens of similar alloy chemistry.

The average reaction completion times, t_f, for the room temperature undeformed and deformed samples were 7 and 6 h, respectively; highlighting that the RT pre-straining influenced the subsequent aging kinetics. This result is consistent with the DSC-based observations that the presence of dislocations in the deformed material enhanced the precipitation process by shifting the exothermic peak to lower temperatures. While the difference in t_f associated with a change in kinetics was approximately 14%, the total heat released differed by less than 6% for both cases. This small difference in total heat released may again be associated with the ratio of precipitate types that form during the aging process (β'' versus Q'). For samples exposed to the 170 °C warm thermal cycle, undeformed and deformed completion times decreased to 5.8 and 5 h and further decreased to 3 and 2.6 h, respectively, for the 230 °C pre-aging condition. The significantly shorter t_f values for both

the undeformed and deformed the 230 °C conditions relative to RT and 170 °C suggests that considerable aging occurred during thermal cycling of the 230 °C conditions. Furthermore, the relatively minor difference in t_f between the undeformed and deformed states shows that temperature exposure was the primary driver for the reduction in time to the peak-aged condition for the 230 °C thermally cycled samples during IC analysis. The IC and DSC results indicate that more precipitates have been formed during the warm forming cycle at 230 °C, which leaves fewer solute atoms available for precipitation during the IC/DSC runs compared to the other conditions.

Although the multi-step aging process consisting of (i) pre-aging at 100 °C, (ii) a short temperature exposure between 220 and 280 °C (*i.e.*, the warm forming cycle), and (iii) a PBC, results in slightly superior toughness and bendability properties than the AA6013-T6 condition, it should be noted that the sensitivity to the actual thermal history during the elevated temperature cycle will need to be addressed by automotive parts manufacturers aiming to produce large numbers of components with tight quality control tolerances. The aging model developed as part of this study can be a useful design tool, as shown by its predictive capability in Fig. 10. Specifically, it can be used to predict the evolution of the volume fraction of precipitates and yield strength at warm forming temperatures, which will be useful when determining heating and paint curing cycles, to a first order of accuracy. As shown through differential scanning and isothermal calorimetry experiments on deformed AA6013-PA material, deformation enhances subsequent precipitation aging kinetics. Consequently, future work should consider deformation effects on aging response in order to develop a more precise prediction of the post-warm formed alloy properties. An example of such

approaches accounting for aging in deformed samples is described by Poole et al. (Ref 52) and would be a logical extension of the model developed here.

4. Summary and Conclusions

- The mechanical properties of AA6013-PA exposed to elevated temperature aging, in the range of 220-280 °C, were determined for a variety of cycle times. Additionally, the secondary aging response due to exposure at 177 °C for 30 min (a simulated automotive paint bake cycle), was examined. Depending on the aging temperature, T6 level mechanical properties could be obtained with a drastically reduced total exposure time (410 s at 235 °C plus 30 min at 177 °C), compared to the conventional T6 aging treatment for AA6xxx alloys ($\sim$ 8 h at 180 °C).
- The precipitation kinetics of AA6013, in a pre-aged starting condition (AA6013-PA), was determined experimentally and a strong obstacle model was used to describe the evolution of yield strength for this alloy as a function of precipitate volume fraction. This model was calibrated between 220 and 280 °C and validated for single-step heat treatments at temperatures of 227 and 243 °C with good correlation to experimental yield strength measurements.
- The calibrated model was also shown to be accurate for multi-step heat treatments consisting of artificial aging followed by exposure to an automotive paint bake cycle. The resulting model can be used to assess warm forming processing routes for AA6013-PA sheet.
- The degree of strain hardening of the AA6013-PA sheet at the warm forming temperature of 230 °C was highly sensitive to a narrow range of times at temperature, with a decay in n-value (hardening exponent) from 0.27 to 0.08 for holding times at 230 °C of 5 and 180 s, respectively.
- The formability of the PA temper was found to decrease with temperature for the 3 min heating times that could be achieved in the current formability testing. It is possible that shorter heating and longer forming cycles could be used to improve the warm formability of the alloy.
- The PA temper showed approximately a 50% improvement in formability compared to the T6 temper at room temperature for plane strain loading. The current data has shown that a relatively short (6-7 min, 235 °C) thermal cycle would serve to impart T6 strength levels to PA components post-forming.
- Deformation at room temperature accelerated the subsequent aging kinetics of AA6013-PA, such that the peak aging time decreased by 14%. Similar trends were observed at elevated temperatures; however, for the 230 °C thermal cycling conditions, temperature was shown to play a larger role than deformation in altering subsequent aging kinetics. This interaction between deformation and subsequent aging is a potential area for future model improvement and should be considered in room-temperature forming of the PA temper when secondary aging is to be prescribed.
- The bendability of AA6013-PA sheet is sensitive to its aged state; however, a final bend angle of 110° can be achieved depending on the warm forming cycle time and temperature. To achieve a bend angle that is beneficial for automotive crash applications, the final condition of the A6013-PA alloy should be in an under-aged (and not T6) state.

References

1. D. Li and A.K. Ghosh, Tensile Deformation Behavior of Aluminum Alloys at Warm Forming Temperatures, *Mater. Sci. Eng. A*, 2003, **352**, p 279–286
2. D. Li and A.K. Ghosh, Biaxial Warm Forming Behavior of Aluminum Sheet Alloys, *J. Mater. Process. Technol.*, 2004, **145**, p 281–293
3. P.J. Bolt, N.A.P.M. Lamboo, and P.J.C.M. Rozier, Feasibility of Warm Drawing of Aluminium Products, *J. Mater. Process. Technol.*, 2001, **115**(1), p 118–121
4. S. DiCecco, C. Butcher, M.J. Worswick, E. Boettcher, E. Chu, and C. Shi, "Determination of Forming Limit Diagrams of AA6013-T6 Aluminum Alloy Sheet Using a Time and Position Dependent Localized Necking Criterion," in Proceedings International Deep Drawing Research Group, IDDRG, Linz, Austria, June 12–15, 2016
5. S. DiCecco, M. Di Ciano, C. Butcher, and M.J. Worswick, "Numerical and Experimental Investigation of the Formability of AA6013-T6", in *Journal of Physics: Conference Series* vol 896 (IOP Publishing, September, 2017), p. 012114
6. S. Mahabunphachai and M. Koç, Investigations on Forming of Aluminum 5052 and 6061 Sheet Alloys at Warm Temperatures, *Mater. Des.(1980-2015)*, 2010, **31**(5), p 2422–2434
7. M. Ghosh, A. Miroux, R.J. Werkhoven, P.J. Bolt, and L.A.I. Kestens, Warm Deep-Drawing and Post Drawing Analysis of Two Al-Mg–Si Alloys, *J. Mater. Process. Technol.*, 2014, **214**(4), p 756–766
8. G. Palumbo, A. Piccininni, P. Guglielmi, D. Sorgente, L.D. Scintilla, and L. Tricarico, Application of the Warm Hydroforming Process to the Manufacturing of Pre-Aged 6xxx series Components Using a Numerical/Experimental Approach, *Key Eng. Mat.*, 2014, **622–623**, p 701–708
9. M. Kumar, C. Poletti, and H.P. Degischerl, "Formability of Heat Treated Al-Mg-Si Alloys", in New Frontiers in Light Metals:

Proceedings of the 11th International Aluminium Conference INALCO 2010. (IOS Press, 2010). p. 251

10. M. Kumar, C. Poletti, and H.P. Degischer, Precipitation Kinetics in Warm Forming of AW-7020 Alloy, *Mater. Sci. Eng. A*, 2013, **561**, p 362–370

11. M. Kumar, N. Sotirov, and C.M. Chimani, Investigations on Warm Forming of AW-7020-T6 Alloy Sheet, *J. Mater. Process. Technol.*, 2014, **218**(8), p 1769–1776

12. M. Kumar and N. Ross, Warm Forming and Paint Bake Response of AW-7xxx Sheet in Various Tempers, *Key Eng. Mat.*, 2015, **651–653**, p 47–52

13. M. Kumar and N.G. Ross, Influence of Temper on the Performance of a High-Strength Al-Zn–Mg Alloy Sheet in the Warm Forming Processing Chain, *J. Mater. Process. Technol.*, 2016, **231**, p 189–198

14. M. Di Ciano, S. DiCecco, S. Esmaeili, M.A. Wells, and M.J. Worswick, Coarsening of AA6013-T6 Precipitates During Sheet Warm Forming Applications, *J. Mater. Eng. Perform.*, 2018, **27**(3), p 939–947

15. K. Omer, A. Abolhasani, S. Kim, T. Nikdejad, C. Butcher, M.A. Wells, S. Esmaeili, and M.J. Worswick, Process Parameters for Hot Stamping of AA7075 and D-7xxx to Achieve High Performance Aged Products, *J. Mater. Process. Technol.*, 2018, **257**, p 170–179

16. S. Esmaeili, D.J. Lloyd, and W.J. Poole, A Yield Strength Model for the Al-Mg-Si-Cu Alloy AA6111, *Acta Mater.*, 2003, **51**, p 2243–2257

17. S. Esmaeili, X. Wang, D.J. Lloyd, and W.J. Poole, On the Precipitation-Hardening Behavior of the Al-Mg-Si-Cu Alloy AA6111, *Metall. Mater. Trans. A*, 2003, **34A**, p 751–763

18. S. Esmaeili and D.J. Lloyd, Effect of Composition on Clustering Reactions in AlMgSi (Cu) Alloys, *Scr. Mater.*, 2004, **50**, p 155–158

19. S. Esmaeili, D. Vaumousse, M. Zandbergen et al., A Study on the Early-Stage Decomposition in the Al-Mg-Si-Cu Alloy AA6111 by Electrical Resistivity and Three-Dimensional Atom Probe, *Philos. Mag.*, 2007, **87**, p 3797–3816

20. S. Pogatscher, H. Antrekowitsch, H. Leitner et al., Influence of the Thermal Route on the Peak-Aged Microstructures in an Al-Mg-Si Aluminum Alloy, *Scr. Mater.*, 2013, **68**, p 158–161

21. M. Liu, B. Klobes, and K. Maier, On the Age-Hardening of an Al-Zn-Mg-Cu Alloy: A Vacancy Perspective, *Scr. Mater.*, 2011, **64**, p 21–24

22. S. Esmaeili, D.J. Lloyd, and W.J. Poole, Modeling of Precipitation Hardening for the Naturally Aged Al-Mg-Si-Cu Alloy AA6111, *Acta Mater.*, 2003, **51**, p 3467–3481

23. X. Wang, S. Esmaeili, and D.J. Lloyd, The Sequence of Precipitation in the Al-Mg-Si-Cu alloy AA6111, *Metall. Mater. Trans. A*, 2006, **37**, p 2691–2699

24. S. Esmaeili and D.J. Lloyd, Modeling of Precipitation Hardening in Pre-Aged AlMgSi (Cu) Alloys, *Acta Mater.*, 2005, **53**, p 5257–5271

25. S. Esmaeili, D.J. Lloyd, and W.J. Poole, Effect of Natural Aging on the Resistivity Evolution During Artificial Aging of the Aluminum Alloy AA6111, *Mater. Lett.*, 2005, **59**, p 575–577

26. C.S.T. Chang and J. Banhart, Low-Temperature Differential Scanning Calorimetry of an Al-Mg-Si alloy, *Metall. Mater. Trans. A*, 2011, **42**(7), p 1960–1964

27. D. Bryant, The Effects of Presaging Treatments on Aging Kinetics and Mechanical Properties in AA6111 Aluminum Autobody Sheet, *Metall. Mater. Trans. A*, 1999, **30**, p 1999–2006

28. J. Banhart, C.S.T. Chang, Z. Liang, N. Wanderka, M.D.H. Lay, and A.J. Hill, Natural Aging in Al-Mg-Si Alloys–A Process of Unexpected Complexity, *Adv. Eng. Mater.*, 2010, **12**(7), p 559–571

29. R.C. Dorward, Preaging Effects in Al-Mg-Si alloys, *Metall. Trans.*, 1973, **4**(2), p 507–512

30. M. Murayama and K. Hono, Pre-precipitate Clusters and Precipitation Processes in Al-Mg-Si Alloys, *Acta Mater.*, 1999, **47**(5), p 1537–1548

31. M. Werinos, H. Antrekowitsch, E. Kozeschnik, T. Ebner, F. Moszner, J.F. Löffler, and S. Pogatscher, Ultrafast Artificial Aging of Al-Mg-Si Alloys, *Scr. Mater.*, 2016, **112**, p 148–151

32. B. Raeisinia, W.J. Poole, X. Wang, and D.J. Lloyd, A Model for Predicting the Yield Stress of AA6111 After Multistep Heat Treatments, *Metall. Mater. Trans. A*, 2006, **37**(4), p 1183–1190

33. W.F. Miao and D.E. Laughlin, Effects of Cu Content and Preaging on Precipitation Characteristics in Aluminum Alloy 6022, *Metall. Mater. Trans. A*, 2000, **31**(2), p 361–371

34. Y.G. An, H. Vegter, L. Zhuang, and A. Hurkmans, Fast Aging Kinetics of the AA6016 Al-Mg-Si Alloy and the Application in Forming Process, *Metall. Mater. Trans. A*, 2006, **33**(10), p 3121–3126

35. M. Kolar, K.O. Pedersen, S. Gulbrandsen-Dahl et al., Effect of Pre-Deformation on Mechanical Response of an Artificially Aged Al-Mg-Si Alloy, *Mater. Trans.*, 2011, **52**, p 1356–1362

36. R.S. Yassar, D.P. Field, and H. Weiland, The Effect of Predeformation on the β''and β′ Precipitates and the Role of Q′ Phase in an Al-Mg-Si Alloy; AA6022, *Scr. Mater.*, 2005, **53**, p 299–303

37. R.S. Yassar, D.P. Field, and H. Weiland, The Effect of Cold Deformation on the Kinetics of the β'' Precipitates in an Al-Mg-Si Alloy, *Metall. Mater. Trans. A*, 2005, **36**, p 2059–2065

38. K. Teichmann, C.D. Marioara, K.O. Pedersen, and K. Marthinsen, The Effect of Simultaneous Deformation and Annealing on the Precipitation Behaviour and Mechanical Properties of an Al-Mg–Si Alloy, *Mater. Sci. Eng. A*, 2013, **565**, p 228–235

39. C. Genevois, D. Fabregue, A. Deschamps, and W.J. Poole, On the Coupling Between Precipitation and Plastic Deformation in Relation with Friction Stir Welding of AA2024 T3 Aluminium Alloy, *Mater. Sci. Eng. A*, 2006, **441**(1–2), p 39–48

40. A. Deschamps, G. Fribourg, Y. Bréchet, J.L. Chemin, and C.R. Hutchinson, In Situ Evaluation of Dynamic Precipitation During Plastic Straining of an Al-Zn–Mg–Cu Alloy, *Acta Mater.*, 2012, **60**(5), p 1905–1916

41. ASTM Standard E1097–12, "Standard Guide for Determination of Various Elements by Direct Current Plasma Atomic Emission Spectrometry", ASTM International, 2012

42. ASTM Standard E8/E8M-11, "Standard Test Methods for Tension Testing of Metallic Materials", ASTM International, 2011

43. R. Phillip, Virtual Strain Gage Size Study, *Exp. Tech.*, 2015, **39**(5), p 1–3

44. R. Marco, P. Lava, F. Pierron, D. Debruyne, and M. Sasso, Effect of DIC Spatial Resolution, Noise and Interpolation Error on Identification Results with the VFM, *Strain*, 2015, **51**(3), p 206–222

45. S. DiCecco, M. Di Ciano, C. Butcher, and M.J. Worswick, Limit Strain Characterization in an Aluminum Die-Quenching Process, *IOP Conf. Ser. Mater. Sci. Eng.*, 2018, **418**, 012035

46. T. Rahmaan, A. Abedini, C. Butcher, N. Pathak, and M.J. Worswick, Investigation into the Shear Stress, Localization and Fracture Behaviour of DP600 and AA5182-O Sheet Metal Alloys Under Elevated Strain Rates, *Int. J. Impact Eng.*, 2017, **108**, p 303–321

47. VDA 238-100: Plate bending test for metallic materials, Verband der Automobilindustrie (VDA), 2017

48. K. Cheong, K. Omer, C. Butcher, R. George, and J. Dykeman, "Evaluation of the VDA 238–100 Tight Radius Bending Test using Digital Image Correlation Strain Measurement," in Journal of Physics: Conference Series vol 896. (IOP Publishing, September 2017), p. 012075

49. T. Kurz, P. Larour, J. Lackner, T. Steck, and G. Jesner, "Press-Hardening of Zinc Coated Steel-Characterization of a New Material for a New Process," in IOP Conference Series: Materials Science and Engineering vol 159, (IOP Publishing, November, 2016), p. 012025

50. S. Esmaeili, *Precipitation hardening behaviour of AA6111*, University of British Columbia, PhD diss., 2002

51. ASM International Handbook Committee, "ASM Handbook, Volume 04: Heat Treating - Heat Treating of Aluminum Alloys," ASM International, Materials Park, Ohio, 1991, p 841–879

52. W.J. Poole, J.A. Sæter, and S. Skjervold, A Model for Predicting the Effect of Deformation After Solution Treatment on the Subsequent Artificial Aging Behavior of AA7030 and AA7108 Alloys, *Metall. Mater. Trans. A*, 2000, **31**(9), p 2327–2338